

# The minimal flow unit in near-wall turbulence

By JAVIER JIMÉNEZ† AND PARVIZ MOIN

Center for Turbulence Research, Stanford University, Stanford, CA 94305, USA and NASA Ames Research Center, Moffett Field, CA 94035, USA

(Received 25 February 1990)

Direct numerical simulations of unsteady channel flow were performed at low to moderate Reynolds numbers on computational boxes chosen small enough so that the flow consists of a doubly periodic (in  $x$  and  $z$ ) array of identical structures. The goal is to isolate the basic flow unit, to study its morphology and dynamics, and to evaluate its contribution to turbulence in fully developed channels. For boxes wider than approximately 100 wall units in the spanwise direction, the flow is turbulent and the low-order turbulence statistics are in good agreement with experiments in the near-wall region. For a narrow range of widths below that threshold, the flow near only one wall remains turbulent, but its statistics are still in fairly good agreement with experimental data when scaled with the local wall stress. For narrower boxes only laminar solutions are found. In all cases, the elementary box contains a single low-velocity streak, consisting of a longitudinal strip on which a thin layer of spanwise vorticity is lifted away from the wall. A fundamental period of intermittency for the regeneration of turbulence is identified, and that process is observed to consist of the wrapping of the wall-layer vorticity around a single inclined longitudinal vortex.

## 1. Introduction

The structure of near-wall turbulence has been extensively investigated over the past thirty years. In the vicinity of the wall, the flow has been found to be highly organized, consisting of regions of high- and low-speed fluid alternating in the spanwise directions (Kline *et al.* 1967; Smith & Metzler 1983). The presence of streamwise vortices and shear layers protruding from the wall have also been documented by various investigators (see for example, Blackwelder & Eckelmann 1979; Johansson, Her & Haritonidis 1987). In the outer layer, hairpin-like vortices have been observed in flow visualization experiments (Head & Bandyopadhyay 1981) and in numerical simulations (Moin & Kim 1985). An extensive collection of recent work on wall turbulence can be found in (Kline & Afgan 1989).

Despite the large effort devoted to the subject, the basic mechanisms for turbulence production and transport in turbulent boundary layers are not well understood. Most of the ‘structure’ research has been devoted to the kinematic aspects, and a complete and consistent dynamical picture is not yet at hand. The primary reason for this lack of understanding is the existence of complex interactions between various structures and between the flow in the near-wall region and that in the outer layer.

The objective of this work is to obtain and analyse solutions of the Navier–Stokes

† Permanent address: School of Aeronautics, U. Politécnica, Madrid, Spain.

equations that represent a more ordered model of wall turbulence than that which is found in natural boundary layers. To be more specific, our objective is to identify the minimal set of structures that are necessary to sustain a turbulent boundary layer, and to construct a flow model consisting of an ordered periodic array of such structures. The primary means by which this model is evaluated is by assessing the degree to which it can successfully predict certain essential turbulent statistical quantities. If the model is successful, one has a significantly simpler and more manageable ‘laboratory’ in which to study the mechanics of wall-bounded flows and in which to test turbulence control strategies. By construction, this simplified model cannot accurately predict some of the higher-order turbulence statistical quantities, including two-point correlation functions. Accurate predictions of such correlations would presumably require a more elaborate stochastic ordering of the basic flow units (as well as smaller scales resulting from their interaction) instead of a doubly periodic one.

The direct numerical simulation technique is used to construct and to test the basic flow unit. The computations reported are not simulations of flows that can be realized in the laboratory but, as will be shown below, they represent a basic building block from which a self-sustained turbulent flow can be constructed. This flow, or at least its low-order statistics, behaves near the wall in much the same manner as the experimental ones. The physical parameters of the simulations and the numerical details are described in §2, followed in §3 by the spatial scaling of the minimal flow module and of the resulting turbulence statistics. In §3 newly discovered asymmetric solutions for the channel flow will also be described. The turbulence regeneration cycle is described in §4, and the structure of the instantaneous vorticity field is presented in §5, followed by a short discussion of our observations to date on the flow dynamics.

## **2. The set-up of the numerical experiments**

This paper describes the result of direct numerical simulations of the initial-value problem for a spatially periodic channel flow. The code used is that described by Kim, Moin & Moser (1987) and is a fully spectral Navier–Stokes integrator, using de-aliased Fourier expansions in the two homogeneous ( $x, z$ ) directions and Tchebichev polynomials in the cross-channel ( $y$ ) coordinate. A sketch of the computational box and of the coordinate system is shown in figure 1. The top and bottom boundaries of the computational box are physical (no-slip) walls, while the boundaries in both the streamwise and the spanwise directions represent the period (fundamental wavelength). The flow does not consist of only the structures inside the computational box, but of a doubly infinite periodic array of such structures, its images, with streamwise and spanwise periods  $\lambda_x$  and  $\lambda_z$ , and cross-channel extent  $2h$ .

The simulation imposes a constant instantaneous volume flux in the  $x$ -direction,

$$Q = \frac{1}{\lambda_z} \int_0^{\lambda_z} \int_{-1}^1 u \, dy \, dz = \frac{4}{3} h U \quad (1)$$

and a zero instantaneous averaged pressure gradient in the spanwise direction, i.e. the pressure is strictly periodic in  $z$ .  $U$  is a reference velocity, which corresponds to the centreline velocity of a laminar parabolic profile with the same volume flux. Throughout this paper we will use the normalization  $U = 1$  and  $h = 1$ . In these units, the laminar value of the vorticity at the wall is  $\omega_z = 2$ .

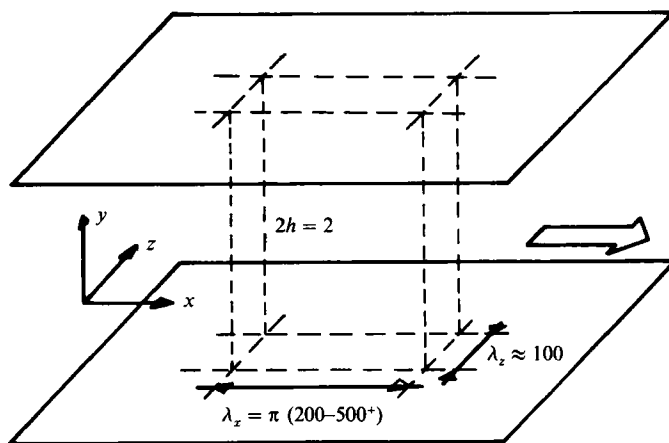


FIGURE 1. Geometry of the computational domain. Note that the simulation is periodic in both the  $x$ - and  $z$ -directions.

As a consequence of condition (1), the streamwise pressure gradient and the spatially averaged instantaneous wall shears,

$$\Omega(\pm 1) = \frac{1}{\lambda_x \lambda_z} \int_0^{\lambda_x} \int_0^{\lambda_z} \frac{\partial u}{\partial y}(x, \pm 1, z) dx dz, \quad (2)$$

vary in time, and they will be used as primary diagnostic quantities on the state of the flow in the neighbourhood of each wall. Time-averaged wall shears are defined as

$$\bar{\Omega}_w(\pm 1) = \bar{\Omega}(\pm 1), \quad (3)$$

where the overbar is the averaging operator over some specified period of time. It will be seen later that the two walls of the channel may behave differently for fairly long periods of time, and the distinction between the two averaged wall shears will be convenient on those occasions. For each particular wall, we can then define local friction velocities and lengthscales,

$$u_r(\pm 1) = (\bar{\Omega}_w \nu)^{\frac{1}{2}}, \quad \delta_r(\pm 1) = (\nu / \bar{\Omega}_w)^{\frac{1}{2}}, \quad (4)$$

and refer velocities and lengths to local wall units in the usual manner,  $u^+ = u/u_r$ , and  $y^+ = y/\delta_r$ . In addition, a local ‘wall’ time can be defined, which is the minimum timescale for events in the wall layer,

$$t^+ = t u_r / \delta_r = \bar{\Omega}_w t. \quad (5)$$

In the rest of the paper, all quantities with a (+) superscript and all primed quantities, such as  $u'$ , should be understood to be expressed in wall units. Because of the constancy of volume flux, the most convenient Reynolds number to characterize the flow is

$$Re = \frac{3Q}{4\nu} = \frac{Uh}{\nu}. \quad (6)$$

The computational grid used for most of the runs was  $32 \times 129 \times 16$  in  $x, y, z$  ( $48 \times 129 \times 24$  before de-aliasing). The spanwise period of the box was varied between 80 and 160 wall units and its streamwise period between 300 and 600, and the

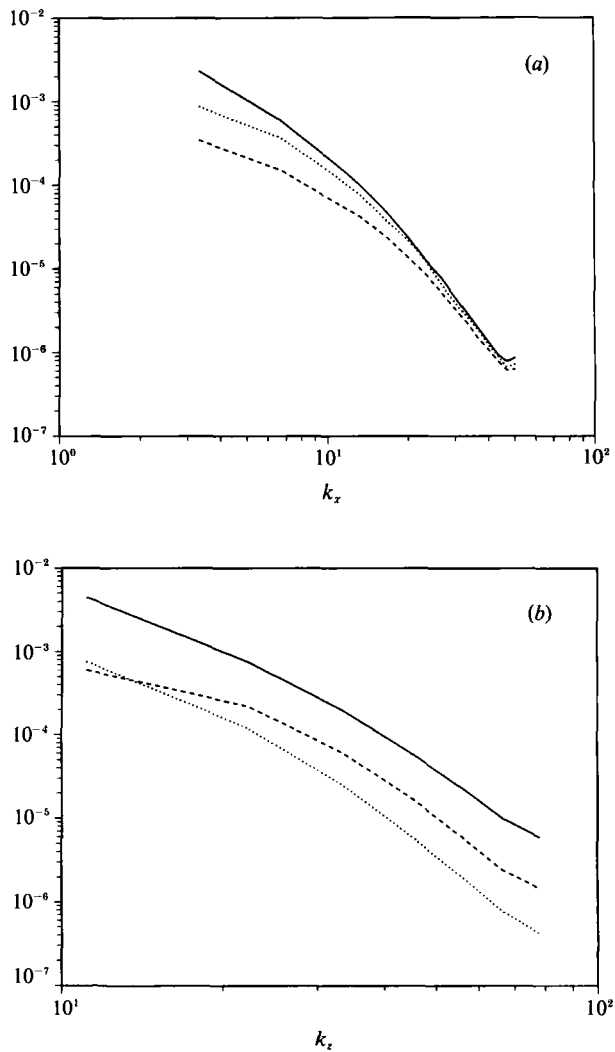


FIGURE 2. Spatial velocity power spectra, along (a) the  $x$ - and (b)  $z$ -axes, at  $y^+ = 34$ .  $Re = 5000$ ,  $\lambda_x = 0.6\pi$ ,  $\lambda_z = 0.18\pi$ . Averaging time for the spectra:  $200h/U$ . Solid line,  $u'$ ; dashed,  $v'$ ; dotted,  $w'$ .

corresponding grid resolution was  $\Delta z^+ = 5-10$  and  $\Delta x^+ = 8-16$ . Especially for the smallest and most interesting boxes, the resolution was comparable to the one used by Kim *et al.* (1987) and was shown there to be sufficient to resolve the essential turbulent scales. A few simulations were run at twice the streamwise resolution, without any apparent change in the qualitative behaviour of the flow or in its low-order statistics. On the other hand, a few runs which were made with only half as much resolution in the spanwise direction did appear slightly underresolved on visual inspection of the flow fields, and were abandoned.

Sample streamwise and spanwise power spectra are shown in figure 2. They correspond to a typical box at the highest Reynolds number,  $Re = 5000$ , but still show acceptable drop-offs at high frequencies, confirming that the small scales are adequately represented. The resolution (accuracy) for smaller boxes or lower Reynolds numbers is correspondingly better. Figure 3 shows the two-point spatial

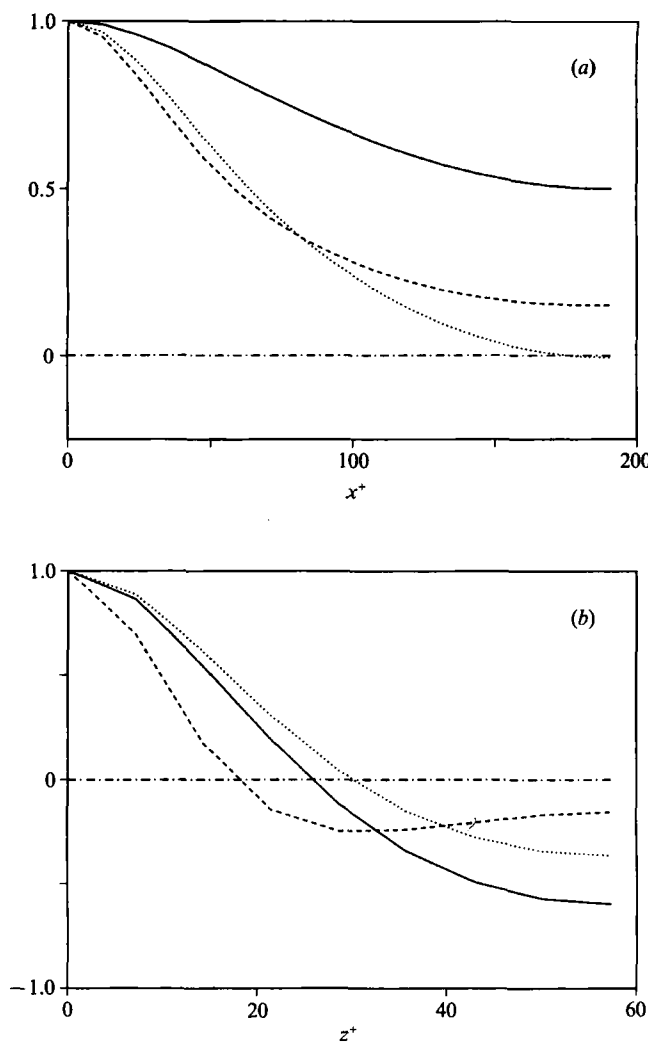


FIGURE 3. Two-point spatial autocorrelation function along (a) the  $x$ - and (b)  $z$ -axes, in the near-wall region ( $y^+ = 7.2$ ). In both cases, the plot spans half of the computational domain. Conditions and symbols as in figure 2.

autocorrelation function for the velocity fields for the same case. Its most striking feature is the lack of a clear decay to zero at the largest separations, demonstrating that the computational box is not large enough for distant points to be uncorrelated and that the flow field consists of a relatively ordered (in fact, strictly periodic) array of identical structures, each of which is relatively coherent in space. This, of course, was the main point of the simulation.

Time was advanced using the second-order Adams–Bashforth scheme for the convective terms and the implicit second-order Crank–Nicholson scheme for the linear viscous terms. The maximum CFL number was kept at approximately 0.2, which can be shown to result in a relative time-marching error for the shortest scales of  $\sim 10^{-3}$  per time step or  $\sim 0.1$  per eddy turnover time. A test run with half the time step revealed no appreciable difference in the results, but the use of a substantially higher CFL number in a comparable code is known to have resulted in spurious chaotic behaviour (Jiménez 1990).

All of the simulations in this paper were run at Reynolds numbers between 2000 and 5000 and on computational boxes that were always shorter than or equal to  $\lambda_x = \pi$ . At these Reynolds numbers, Poiseuille flow is stable to infinitesimal perturbations, and any sustained turbulence is subcritical. Under these circumstances the question of initial conditions may become important, and the procedure chosen in this investigation was to start the flow for each combination of  $Re$  and wavelengths using as initial conditions the fully developed flow field from a nearby combination of parameters. The very first run was initiated as an essentially random finite-amplitude perturbation of the parabolic flow at a fairly large Reynolds number ( $Re = 7000$ ), and subsequent runs were started incrementally from the results of that simulation.

Since our aim was to determine the absence or existence of solutions for certain parameter ranges, this procedure was checked with some care. The flow parameters were always changed as little as practical from one run to the next, and the question of the independence of the solutions from their initial conditions was tested several times. This was done by reproducing the same flow starting from different initial conditions (corresponding to different combinations of parameters, some closer than others to the final combination). In particular, when crossing parameter boundaries between the different observed flow regimes, the possibility of hysteresis was investigated by approaching a given parameter combination from initial conditions corresponding to flows in different regimes. In all cases the simulation was allowed to run for a long time, until no apparent change in either the statistics or the qualitative flow behaviour was apparent. On no occasion did the long-term behaviour depend on the initial conditions, although the rate at which the final state was approached did depend on the difference between the final parameters of the flow and those corresponding to the initial state.

The desire to observe only statistically stationary flow regimes led to the need for long integration times. There are several intrinsic timescales in the flow. The eddy turnover time in the dimensionless time units based on  $U$  and  $h$  is  $T = O(1)$ . The viscous timescale in the sublayer is the wall unit,  $O(1/\Omega_w) = O(1/10)$ . The viscous timescale associated with the outer flow is much longer,  $O(Re)$ , and it appears in the simulation as a slow relaxation of the statistics in scales  $T = O(1000)$ . An additional, very important, intermediate timescale,  $T = O(100)$ , which is characterized by an  $O(1)$ , oscillation of the flow statistics, was discovered during this investigation. This latter timescale, together with the viscous relaxation, required running times of the order of 1000–3000 before a particular flow could be considered asymptotically steady, especially at the higher Reynolds numbers. This corresponds to  $3\text{--}4 \times 10^5$  time steps, and was possible only because of the relatively fast execution times associated with the small domains used in the simulation, which allowed good spatial resolution using relatively few spectral modes. Still, each time step required 0.7 s on a Cray Y-MP, requiring between 50 and 100 CPU hours for each of the simulations in which turbulence was sustained and the flow was followed long enough to establish its asymptotic behaviour.

### **3. Box minimization and statistical properties**

Three relatively low Reynolds numbers were analysed: 2000, 3000 and 5000. The lowest one is generally considered transitional by most investigators, although some form of turbulence can be sustained at much lower Reynolds numbers ( $\sim 1000$ ), and large-scale intermittency disappears at  $Re \approx 1800$  (Patel & Head 1969; Nishioka &

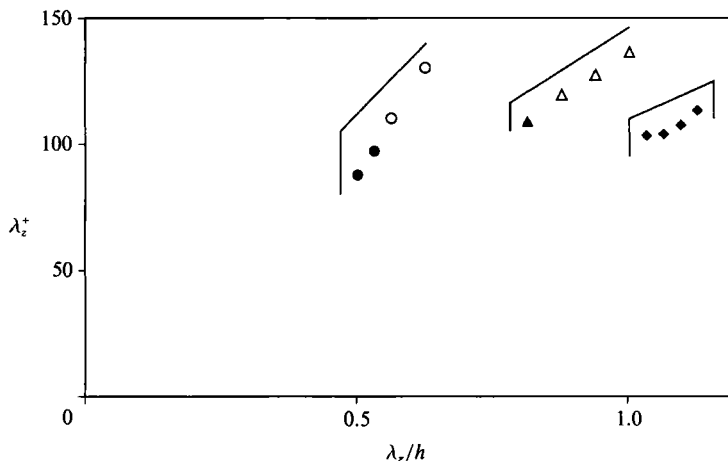


FIGURE 4. Spanwise wavelength of the computational box in wall and absolute units. vertical lines mark limits at which simulations could not be sustained:  $\diamond$ ,  $Re = 2000$ ;  $\triangle$ ,  $Re = 3000$ ;  $\circ$ ,  $Re = 5000$ . Open symbols are two-walled turbulence, closed symbols are one-walled (see §3.3). All simulations use  $\lambda_x = \pi$ . Inclined lines just bracket related data.

Asai 1985). On the other hand, most authors agree that channel flow is fully developed above  $Re = 3000$ –3800 (Eckelmann 1974). For each Reynolds number, we sought the smallest computational box that would sustain ‘turbulence’ indefinitely. The basic requirement was that the flow remained non-laminar, stochastic and three-dimensional. Note that most of the effort was spent locating the lower boundary of the domain size rather than the upper-critical boundary which, as it turned out, existed at  $Re = 2000$ .

### 3.1. Scaling of the minimal domain

A detailed fine-tuning of the spanwise dimension of the box was made at the streamwise length of  $\pi h$ . This streamwise wavelength was selected as an immediate value between two numerical experiments with lengths  $2\pi h$  and  $\frac{1}{2}\pi h$ . In the latter case turbulent fluctuations decayed, whereas in the former the box contained several structures. For each Reynolds number in figure 4, the spanwise dimension of the computational box, measured in wall units, is plotted against its value measured in outer units. The vertical lines mark the boundaries beyond which no turbulent flow could be maintained. It can be seen that the critical channel span varies for different Reynolds numbers when expressed in outer units but is roughly the same in wall units. The critical value is around  $\lambda_z^+ = 100$  or, more precisely, between 85 and 110. This is in very good agreement with the experimentally measured mean streak spacing in the viscous sublayer reported by Smith & Metzler (1983) who also found slightly lower spacings at higher Reynolds numbers. The coincidence of the lower critical value for the spanwise width of the computational box and the accepted mean value for the streak spacing provides a dynamical significance to the latter quantity. A number of investigators, mostly using hydrodynamic stability analysis, have discussed the significance of the universal mean streak spacing in turbulent boundary layers (e.g. Zhang & Lilley 1981; Jang, Benney & Gran 1986). Present results provide strong evidence for its dynamical importance.

Three less detailed surveys were also conducted to determine the minimum streamwise length at each Reynolds number for a value of  $\lambda_z$  slightly above its minimal value. Plots of  $\lambda_z^+$  vs.  $\lambda_z/h$  for each Reynolds number are shown in figure 5. There appears to be a minimal streamwise period of about  $\lambda_z^+ \approx 250$ –350, which

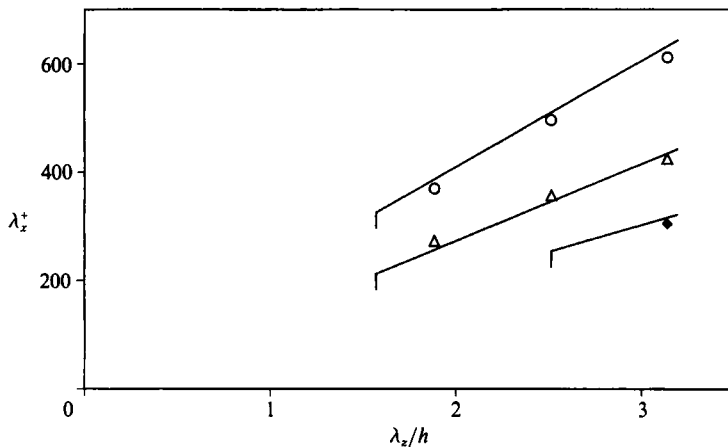


FIGURE 5. Computational box streamwise length in wall and absolute units. Vertical lines mark limits at which simulations could not be sustained.  $\diamond$ ,  $Re = 2000$ ,  $\lambda_z = 0.34\pi$ ;  $\triangle$ ,  $Re = 3000$ ,  $\lambda_z = 0.30\pi$ ;  $\circ$ ,  $Re = 5000$ ,  $\lambda_z = 0.18\pi$ . Open and closed symbols as in figure 4.

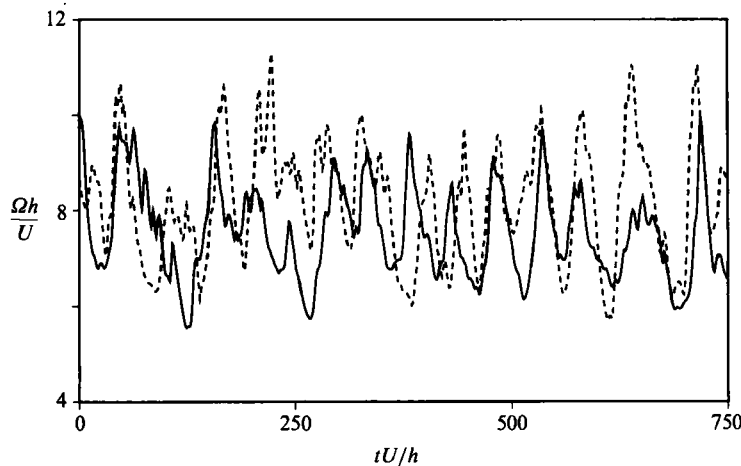


FIGURE 6. Instantaneous averaged wall-shear history for a minimal turbulent channel. Initial transients have been discarded. Only one wall is represented.  $Re = 5000$ . Solid line:  $\lambda_x \times \lambda_z = \pi \times 0.18\pi$ ; dashed:  $0.5\pi \times 0.18\pi$ .

becomes shorter as the Reynolds number increases, although a detailed survey covering both  $\lambda_z$  and  $\lambda_x$  would be needed to decide whether it scales in inner or other variables. Apparently, this is the lower bound for the streamwise length of the eddies in the wall layer, or for the minimum streamwise spacing between eddies of dynamical significance. It is remarkably near to the value of 440 for the mean spacing of vortical structures in the wall region reported by Clark & Markland (1971), as well as to the spacing between substructures within turbulent boundary layer spots,  $\lambda_z^+ \approx 200-500$ , reported by various investigators (see Sankaran, Sokolov & Antonia 1988, and references therein).

### 3.2. Sample statistics

A time history of the plane-averaged shear,  $\Omega$ , on one wall is shown in figure 6. Stochastic and intermittent behaviour of the wall shear stress is clearly discernible. The intermittency is prominently exposed by the limited size of the computational

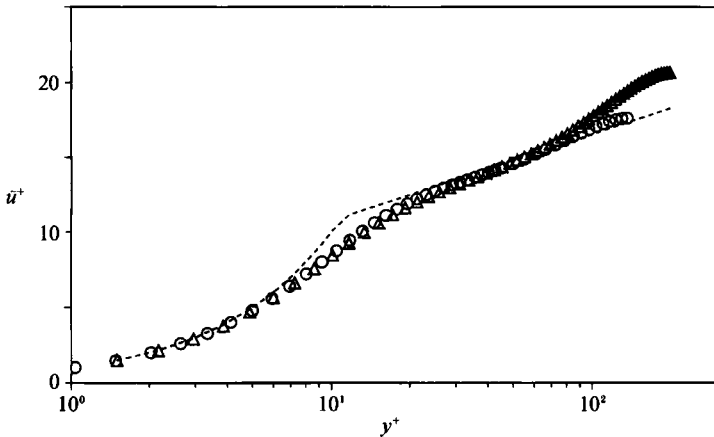


FIGURE 7. Mean streamwise velocity near the wall.  $\circ$ ,  $Re = 3000$ ,  $\lambda_x \times \lambda_z = \pi \times 0.30\pi$ ;  $\triangle$ ,  $Re = 5000$ ,  $\lambda_x \times \lambda_z = 0.6\pi \times 0.18\pi$ . Dashed line is  $\bar{u}^+ = 2.5 \log y^+ + 5$ .

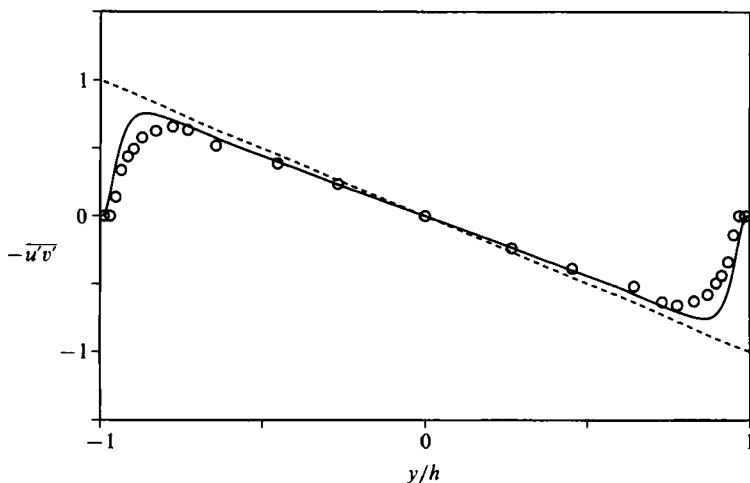


FIGURE 8. Reynolds shear stress normalized with the shear velocity.  $Re = 5000$ ,  $\lambda_x \times \lambda_z = 0.6\pi \times 0.18\pi$ . Solid line:  $-\bar{u}'\bar{v}'$ ; dashed:  $-\bar{u}'\bar{v}' + (1/Re) \partial \bar{u} / \partial y$ . Symbols from Wei & Willmarth (1989),  $Re \approx 3850$ .

box in the  $(x, z)$ -plane and the correspondingly small statistical sample. With a very large computational box, the spatial averaging in equation (2) would have involved several eddies and the temporal fluctuations in figure 6 would have been significantly reduced. The equivalent cancellation of fluctuations for this small box involves averaging the behaviour of a single structure over a long time. The statistical quantities in the remainder of this section were obtained using plane and time averaging, which will be denoted by an overbar as in equation (3).

Mean velocity,  $\bar{u}^+$ , profiles for Reynolds numbers 3000 and 5000 are shown in figure 7. The profile for the  $Re = 3000$  case is in excellent agreement with the standard logarithmic law for turbulent channel flow, while the one for  $Re = 5000$  is in good agreement in the inner region but exhibits only a minimal log layer and a wake region which is uncharacteristic of channels. At this latter Reynolds number, the typical

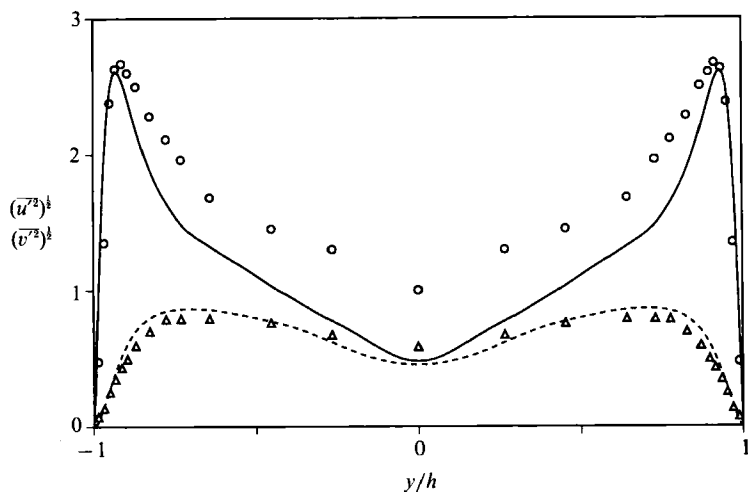


FIGURE 9. Root-mean-square velocity fluctuations normalized by the wall shear velocity, in global coordinates. Solid line:  $(\bar{u}'^2)^{1/2}$ ; dashed:  $(\bar{v}'^2)^{1/2}$ .  $Re = 5000, 0.6\pi \times 0.18\pi$ . Symbols are experimental values from Wei & Willmarth (1989) at  $Re \approx 3850$ :  $\circ$ ,  $(\bar{u}'^2)^{1/2}$ ;  $\triangle$ ,  $(\bar{v}'^2)^{1/2}$ . (Wei & Willmarth did not measure  $(\bar{w}'^2)^{1/2}$ ).

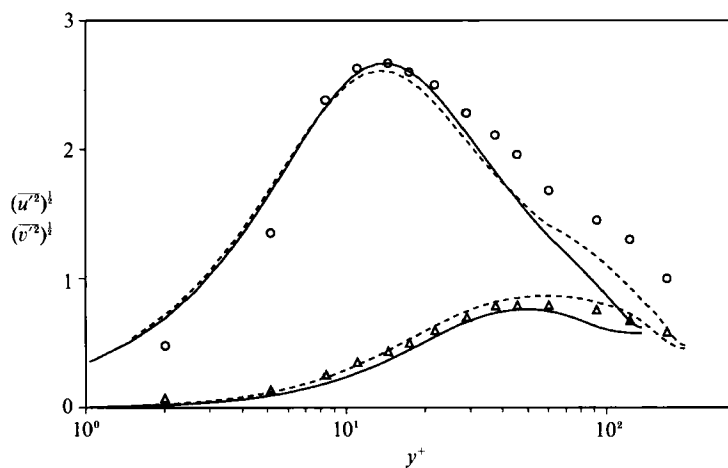


FIGURE 10. Near-wall turbulent intensities in wall coordinates. Solid lines:  $Re = 3000, \lambda_z \times \lambda_z = \pi \times 0.3\pi$ ; dashed:  $Re = 5000, 0.6\pi \times 0.18\pi$ . Symbols as in figure 9.

spanwise box width,  $\lambda_z^+ = 100$ , corresponds in outer coordinates to  $\lambda_z/h = 0.5$ . This is apparently too small to accommodate some of the large-scale structures present in the outer layer and leads to this and other abnormalities in the statistics in that part of the flow. The standard derivation of the logarithmic velocity profile involves the interplay of eddies whose extent normal to the wall scales with their distance from it. One would expect that a constrained spanwise size would also alter their  $y$ -extent and that would in turn disturb the logarithmic region.

In figure 8 the Reynolds shear stress,  $-\bar{u}'\bar{v}'$ , and total stress profiles,  $-\bar{u}'\bar{v}' + (1/Re)\partial\bar{u}/\partial y$ , show that the flow has reached statistically steady state. Turbulent intensities are shown in figures 9 and 10, including the recent measurements of Wei & Willmarth (1989) at a Reynolds number intermediate between the two simulations.

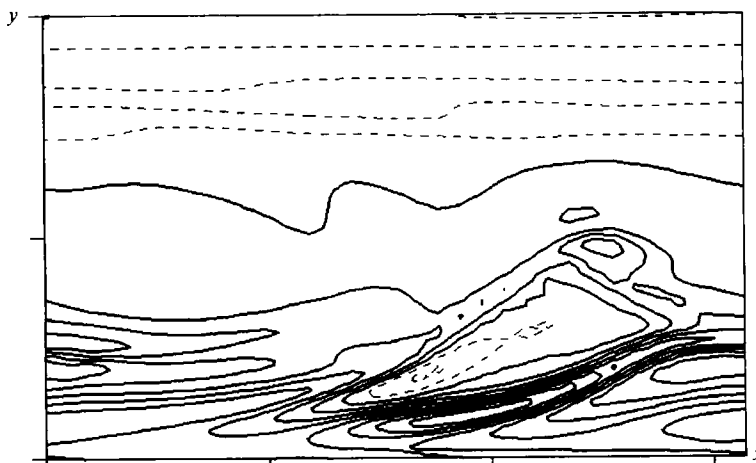


FIGURE 11. Instantaneous  $\omega_z$  map for an  $(x, y)$  section of a one-sided turbulent channel. Note different levels of activity near both walls.  $Re = 2000$ ,  $\pi \times 0.35\pi$ . Isolines increment : 0.5; solid lines :  $\omega_z \leq 0$ .

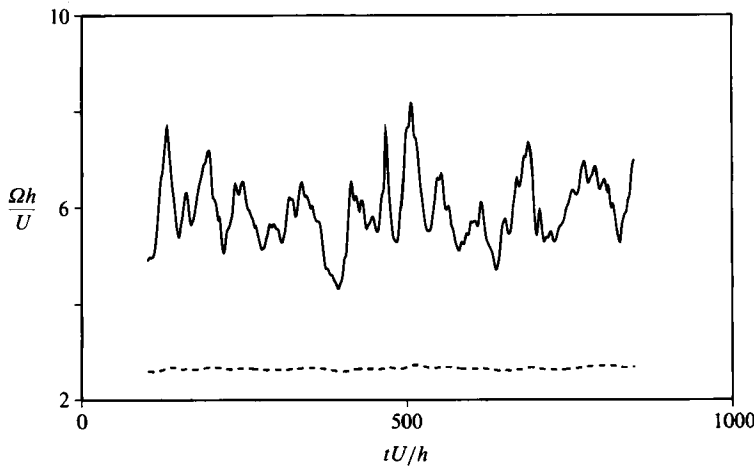


FIGURE 12. Instantaneous averaged wall-shear histories at the upper and lower wall of a one-sided turbulent channel. Initial transients have been discarded.  $Re = 3000$ ,  $\lambda_x = \pi$ ,  $\lambda_z = 0.26\pi$ .  $\Omega h/U = 2$  corresponds to laminar flow. Solid line: lower (active) wall; dashed: upper (quiet).

Near the wall the agreement with the experimental data is very good, while in the outer layer there are large discrepancies, due most probably to the constraining effect mentioned above.

### 3.3. One-sided turbulent channel flow

One of the most interesting observations in this work was the existence of stable states in the channel in which turbulent flow existed only near one wall. This was the predominant state for the three Reynolds numbers studied when the span of the computational box was near its minimal value, and it was the only state observed at  $Re = 2000$ . Contours of the spanwise vorticity,  $\omega_z$ , in an  $(x, y)$ -plane are shown for the latter case in figure 11. Turbulence is clearly confined to near the lower wall, but the flow near the upper one is not steady; it has a small temporal variation but is nearly two-dimensional (see figure 12 and the global profiles in figure 14).

Occasionally, the turbulent state was observed to shift from one wall to the other.

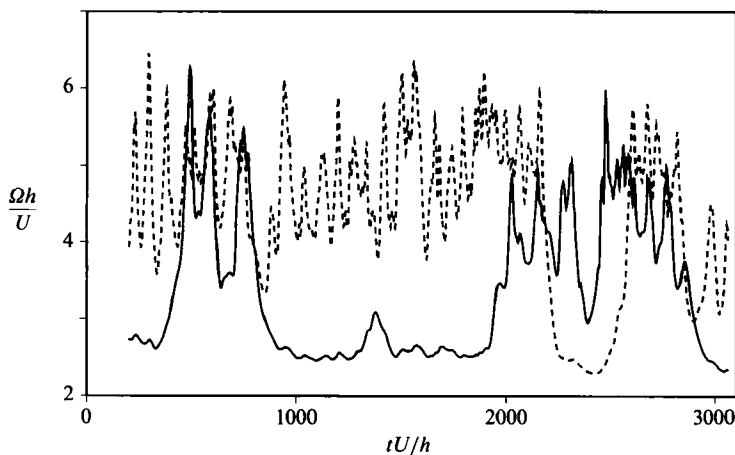


FIGURE 13. Averaged wall-shear histories at the upper and lower walls in a predominantly one-sided turbulent channel. Note that total time is three times longer than in figure 12.  $Re = 2000$ ,  $\lambda_x = \pi$ ,  $\lambda_z = 0.35\pi$ .

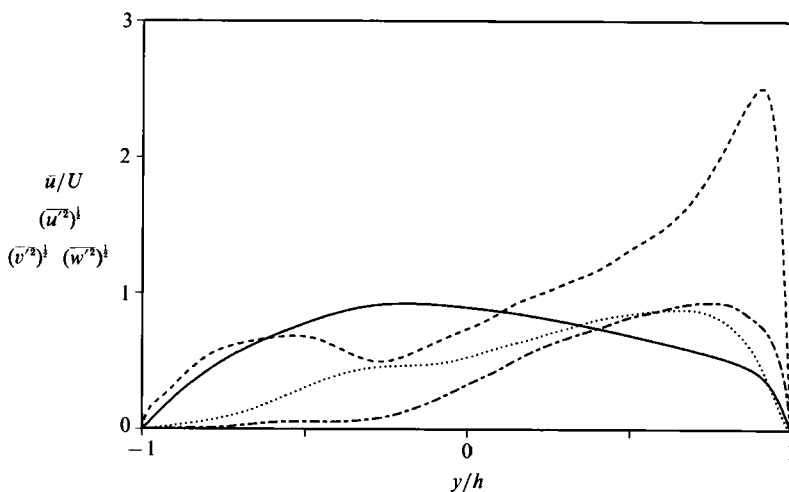


FIGURE 14. Root-mean-square velocity fluctuations normalized by the wall shear velocity, in global coordinates, for a predominantly one-sided channel. Average includes only periods in which turbulence resides near the wall represented here. Solid line:  $\bar{u}/U$ ; dashed:  $(\bar{u}'^2)^{1/2}$ ; dotted:  $(\bar{v}'^2)^{1/2}$ ; dot-dashed:  $(\bar{w}'^2)^{1/2}$ .  $Re = 5000$ ,  $\pi \times 0.16\pi$ . Turbulent intensities are expressed in wall units.

When this happened, the ‘quiet’ wall underwent transition and for a while both walls were turbulent (figure 13). However, this state was not stable, and in a relatively short time turbulence at one of the walls decayed. This transition process was not studied in great detail, but the visualization of a few flow fields suggests that it corresponds essentially to the  $\Lambda$ -vortex mediated laminar–turbulent transition described, for example, by Kleiser & Laurien (1985).

The switching of the active walls was a relatively rare event with a very long characteristic time ( $tU/h \approx 1000$ ). Between those occasions, the flow remained essentially one sided. As far as we are aware, one-sided turbulent channels have never been observed experimentally, although our results suggest that they might occur

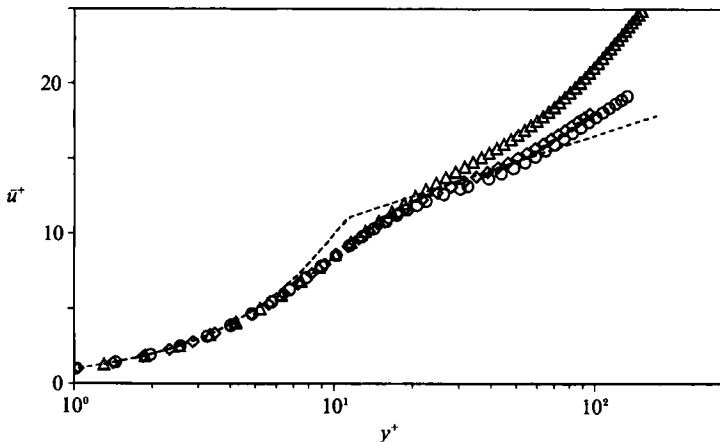


FIGURE 15. Averaged velocities near turbulent wall on one-sided channels. Average includes only periods in which turbulence resides near the wall represented here.  $\diamond$ ,  $Re = 2000$ ,  $\pi \times 0.33\pi$ ;  $\circ$ ,  $Re = 3000$ ,  $\pi \times 0.26\pi$ ;  $\triangle$ ,  $Re = 5000$ ,  $\pi \times 0.16\pi$ . Dashed line is  $u^+ = 2.5 \log y^+ + 5$ .

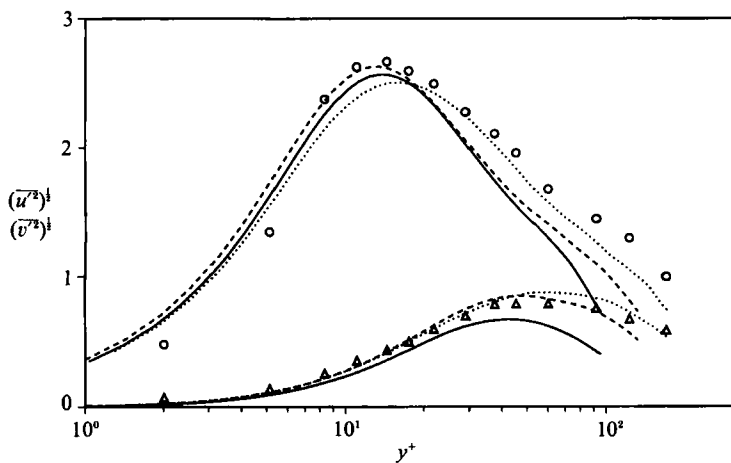


FIGURE 16. Fluctuating intensities corresponding to runs and conditions in figure 15. Solid lines:  $Re = 2000$ ,  $\pi \times 0.33\pi$ ; dashed:  $Re = 3000$ ,  $\pi \times 0.26\pi$ ; dotted:  $Re = 5000$ ,  $\pi \times 0.16\pi$ . Symbols from Wei & Willmarth (1989) as in figure 9.

naturally at low Reynolds numbers. However, some related numerical results have been previously encountered in the context of transition. On the basis of secondary stability theory, Herbert (1983) observes that the subharmonic mode for transition in a channel should occur on a single wall at a time, and May & Kleiser (1985) have observed this feature in direct numerical simulations of transitional channels. The growth rates of the turbulent intensities when the turbulence switches between walls agree approximately with Herbert's most unstable eigenvalue. On the other hand, the switching period between walls seems to correspond to a different phenomenon, occurring at essentially random times, on a scale of the order of the viscous time,  $O(Re)$ .

The mean velocity and intensity profiles for one-sided channels at Reynolds numbers from 2000 to 5000 are shown in figures 14–16. The asymmetry of the profiles is apparent in the linear plots of figure 14, as is the two-dimensionality of the quiet

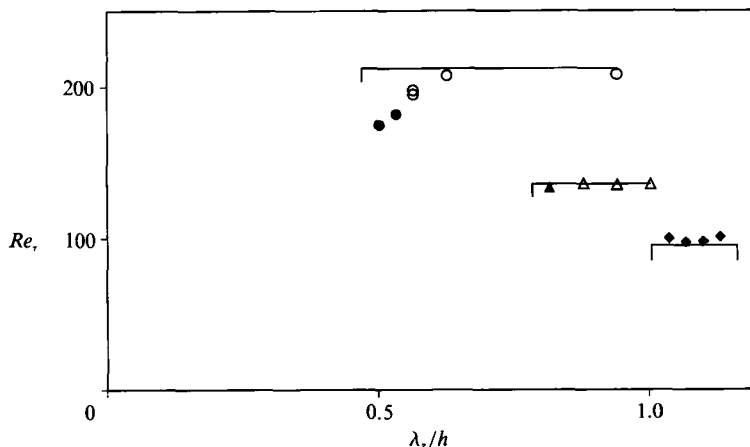


FIGURE 17. Time-averaged wall stress, measured as  $Re_r$ , vs.  $\lambda_z$  and Reynolds number. Symbols are as in figure 4, but some data points here have  $\lambda_z \neq \pi$ . Lines are experimental correlations from Dean (1978).

wall that is implied by the small values of  $(\overline{w'^2})^{1/2}$ . Of interest is the disappearance of the logarithmic layer (figure 15) at  $Re = 5000$ , which is here even more complete than in the two-sided case (see §3.2). Even more noteworthy is the fact that the turbulent intensities in the near-wall region are generally still in good agreement with the experimental data (figure 16) even in the presence of a severely disturbed outer layer which, as in the case of two sided turbulent channels, agrees poorly with experimental data. However, the Reynolds-number effect clearly apparent in the outer part of the layer is in agreement with a similar trend observed by Wei & Willmarth (1989). In experiments ranging from  $Re = 3850$  to 53000.

### 3.4. Wall stresses

Another standard measure of the adequacy of the simulated turbulent channel flow is its conformity to Dean's (1978) correlation. Using numerous experimental data, Dean found an empirical correlation between the wall skin friction and the bulk velocity in turbulent channel flows. The Reynolds number based on shear velocity,  $Re_r = u_r h / \nu$ , is shown for all the computational cases in figure 17. The lines are from Dean's formula, and different symbols are used for two-sided (open symbols) and asymmetric (closed symbols) turbulent computations. For each Reynolds number, results are shown for the different spanwise dimensions of the computational box. Except for the three narrowest cases at the highest Reynolds number,  $Re = 5000$ , the numerical results are in remarkably good agreement with the experimental data. The cases that do not agree with Dean's correlation are those that lack a significant logarithmic layer in the mean velocity profile.

In summary, low-order single-point turbulence statistics in the wall region are accurately predicted in the minimal channel simulations so long as at least the inner portion of the logarithmic layer is reproduced. The outer portion of the boundary layer does not appear to have significant influence on the inner-layer statistics (even in the extreme cases in which only one wall was turbulent). This is consistent with the idea that the logarithmic layer is the region of overlap between the inner and outer regions. The fact that the minimal channel faithfully reproduces many important features of the 'natural' channel is indeed surprising and may have

profound implications. It suggests that the basic turbulence dynamics in the wall region is confined to a rather small region in space. The minimal channel imposes a periodic order surrounding the basic volume, and the results show that this periodic model, in which most of the long-range interactions have been neglected, retains enough structure to reproduce at least the low-order statistical quantities in this region. On the other hand, it is certainly conceivable that other elementary flow units, or other long-range orderings, can lead to similar statistical behaviour.

Owing to its physical simplicity and to the small computational effort required, when compared to the full-scale simulation of natural channels, the minimal channel is an ideal laboratory to study the dynamics and structure of wall-bounded flows and to test wall boundary conditions for turbulence control applications.

#### 4. Intermittency

We have shown that the minimal channel reproduces several of the statistical properties of natural turbulent flows in the near-wall region, while providing a relatively compact computational model. It is a much simpler system than either the numerical simulation of a full-sized channel or a real experiment and provides the opportunity to observe individual turbulent structures in an idealized setting, making them much simpler to study and to analyse. It provides some hope of analysing wall turbulence in the same quasi-deterministic spirit that has been common for some time in free-shear flows. At least two potentially important ingredients are absent from these simulations. First the random occurrence in space and time of structures in natural turbulent wall layers has been replaced by a periodic order. Second, the flow in the outer layer and its influence on near-wall events are not adequately modelled (as shown in the previous section). The statistical results of the previous section suggest that the first effect is not important, while the second has some effect on the wall shear levels and on the structure of the flow above  $y^+ \approx 30$ , but only when it is strong enough that the logarithmic region is cancelled.

In this and the following section we shall study the structure of the near-wall region of the minimal channel using flow-field visualizations of individual events and time sequences of those events. Enough fields have been observed to give some confidence that the features described here are representative of a large percentage of the time in the minimal channel. Whether or not they are representative of events in natural flows will have to be established later by a comparison with full-scale simulations.

The most striking characteristic of the time histories in figures 6, 12, and 13 is their high degree of fluctuations. The plane-averaged wall shear oscillates by a factor of almost two and does so, moreover, in a random but quasi-periodic fashion. During the active periods of this cycle, it is not only the wall stress that ‘blooms’, but all the flow statistics as well. Figure 18 is an enlarged plot of two of the periods in figure 13, showing the averaged wall shear, maximum values of the three vorticity components, both close to and away from the wall, and the instantaneous Reynolds stress,  $-u'v'$ . These maxima are taken over the whole computational box and measure the maximum activity *anywhere* in the flow. It is clear that all of the quantities reach a maximum during the same part of the intermittency cycle, especially below  $y^+ = 10$ . It is interesting to compare the Reynolds stress values in figure 18 with the averaged profile in figure 8. The maximum values encountered here are, even in the quiescent phases, an order of magnitude larger than the averaged values in the profile. The experimental definition of a ‘burst’ has been often taken as a region of the flow in

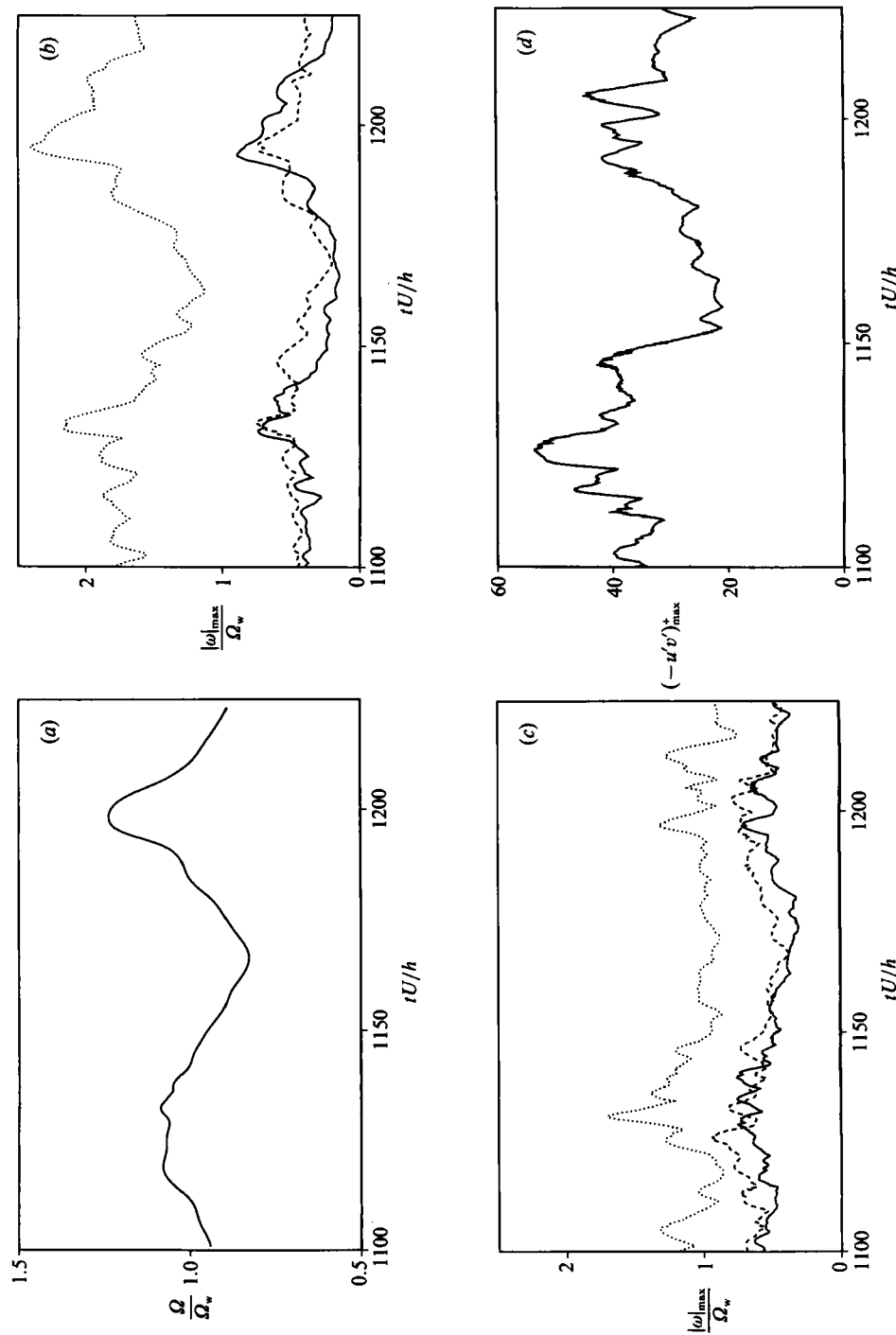


FIGURE 18. Time evolution of flow quantities through two intermittency cycles, in wall variables. Conditions are as in figure 13. (a) Turbulent wall-averaged shear. (b) Maximum magnitude of vorticity components in  $0 \leq y^* \leq 10$ , near the turbulent wall; solid line:  $|\omega_z|$ ; dashed:  $|\omega_y|$ ; dotted:  $|\omega_x|$ . (c) Same as (b), but for  $y^* > 10$ . (d) Maximum Reynolds stress in the turbulent side of the channel.

which the Reynolds stress (or its second-quadrant component) is larger than the averaged value (Bogard & Tiederman 1986). The large ratio of the instantaneous maximum value to the average value suggests that, from the point of view of experimental measurements, some point of the flow is always ‘bursting’. The bursting phenomenon reported by experimental investigators is simply the passage of these active regions past the measurement point (see also Kim & Moin 1986; Moin 1987).

From this point of view, the intermittency cycle that we are studying is a modulation of the bursting activity in time and corresponds to a different phenomenon. Its details will be studied in the next section by visualizations of the flow field; here we shall just discuss its temporal behaviour. A simple counting of peaks in any of the shear histories shows that the basic time period of the intermittency cycle is  $UT/h = O(100)$ . None of the records generated in our simulations contains more than  $\sim 30$  periods, and this precludes a more precise measurement of the timescale. Power spectra of the time series suggest that the period increases with decreasing Reynolds number. The length of the data records is not sufficient to permit a more definite statement on the length of the period or to speculate on possible scaling properties, but the trend is clear and is confirmed by visual inspection of the time records. This is a very long timescale, difficult to reconcile with any obvious property of the flow or of the simulation. In the global units used above it represents many eddy turnover times. In viscous wall units, the different values are slightly more uniform, but they still range from  $\Omega_w T \approx 600$  to 1500.

The residence time of an eddy in the computational box is roughly  $UT_r/h = \lambda_x/h \approx 1.5\text{--}3$  and is quite different from the intermittency period. Since the flow is spatially periodic, this timescale should not appear in the results except by way of some numerical error, and it was therefore tested with some care. In figure 6, the two traces represent identical flows but with streamwise computational box lengths that differ by a factor of two. No appreciable difference in the periods can be observed, making it unlikely that the intermittency observed here is a numerical effect connected to the periodic boundary conditions.

Whatever the mechanism for this cycle is, it appears to be local to each wall. The correlation coefficient between the shear histories at the two walls of a single channel,  $\Omega(1)$  and  $\Omega(-1)$ , is always small,  $|corr| \leq 0.15$ , when both walls are turbulent, indicating that the intermittency cycle acts independently at each wall. In contrast, when only one wall is turbulent, that correlation is larger,  $corr \approx -0.8$ , suggesting that the small excursions of the shear in the quiet wall are passive responses to the activity in the turbulent one. Note that the correlation would be zero if one wall was steady and laminar.

Figure 19 shows the decay of wall shear in a computational box which was initialized from a sustained turbulence condition, but with a spanwise width too small to continue to sustain turbulence. It is interesting to note that the intermittency cycle is still present and that the peaks of each cycle seem to have roughly the same magnitude as in the self-sustaining flow. Each time the wall ‘blooms’ it does so in full force, and even the rate of decay of the wall shear after each event is roughly the same as in the sustained case. The quiescent states to which it decays between bursts become more two-dimensional and closer to laminar, and it takes longer for the activity to regenerate. When finally one event fails to materialize, the flow decays rapidly to a laminar state. This suggests that each of the intermittent events regenerates the turbulent activity in the neighbourhood of one

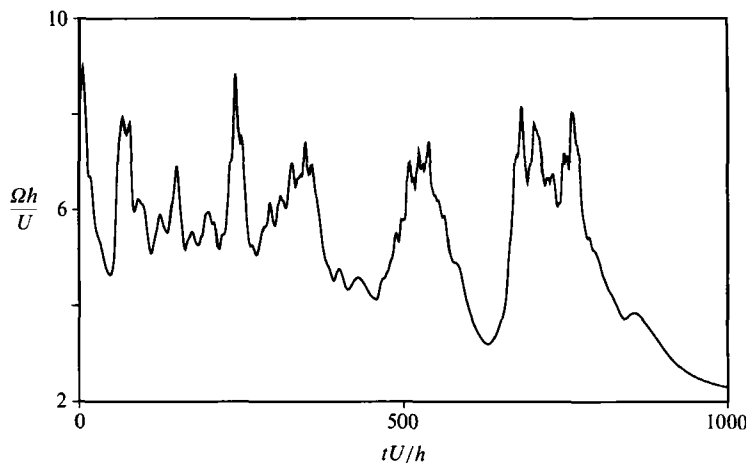


FIGURE 19. Wall-shear history for a decaying minimal turbulent channel. Only one wall is represented.  $Re = 5000, \pi \times 0.15\pi$ . Flow was initialized from the asymptotic solution in a  $\pi \times 0.16\pi$  box.

wall and that the rest of the cycle, at least in that region, is simply the decay of this activity. In the following section we examine the structure of the wall region and its dynamics during the intermittency cycle.

## 5. The structure of the vorticity field

We will concentrate here on the instantaneous structure of the vorticity field, particularly at  $Re = 2000$ , at which the flow is turbulent at only one wall. This value was chosen because the flow features are ‘cleaner’ at low Reynolds numbers but, as mentioned below, similar features are observed at higher  $Re$ , and in cases in which both walls are turbulent. The field that we will describe corresponds to  $Ut/h = 1187$  in the simulation used in the previous section (figure 18) to study the intermittency cycle. Flow fields for that particular sequence, extending from  $Ut/h = 1100$  to 1225, were stored at time increments  $U\delta t/h = 3$ , and analysed visually. The results from all of these flow fields were consistent with the one described here, although there were some variations of the relative strength of the different flow elements during the intermittency cycle. Those variations will be described later in this section, but the structure that we will discuss below can be considered typical of the whole cycle. An earlier analysis of a similar one-sided flow (at  $Re = 7000$ ) was presented in Jiménez (1988) with basically similar results. In addition, three other time sequences of two-sided turbulent channels, at  $Re = 3000$  and 5000, were also stored and analysed (at a somewhat lower temporal resolution) with entirely consistent results. In all of these cases, the flow fields were found to contain the main structural ingredients (sublayer streaks, streamwise vorticity, and near-wall shear layers) observed by previous investigators in the near-wall region, both experimentally and in numerical simulations. The main difference is that, in contrast with previous observations, our computational box contains a single or, at most, two distinct copies of each of those elements.

Figure 20 shows contours of the three vorticity components in an  $(x, z)$ -plane near the wall. The maps for  $\omega_z$  and  $\omega_y$  clearly show the presence of a single low-velocity

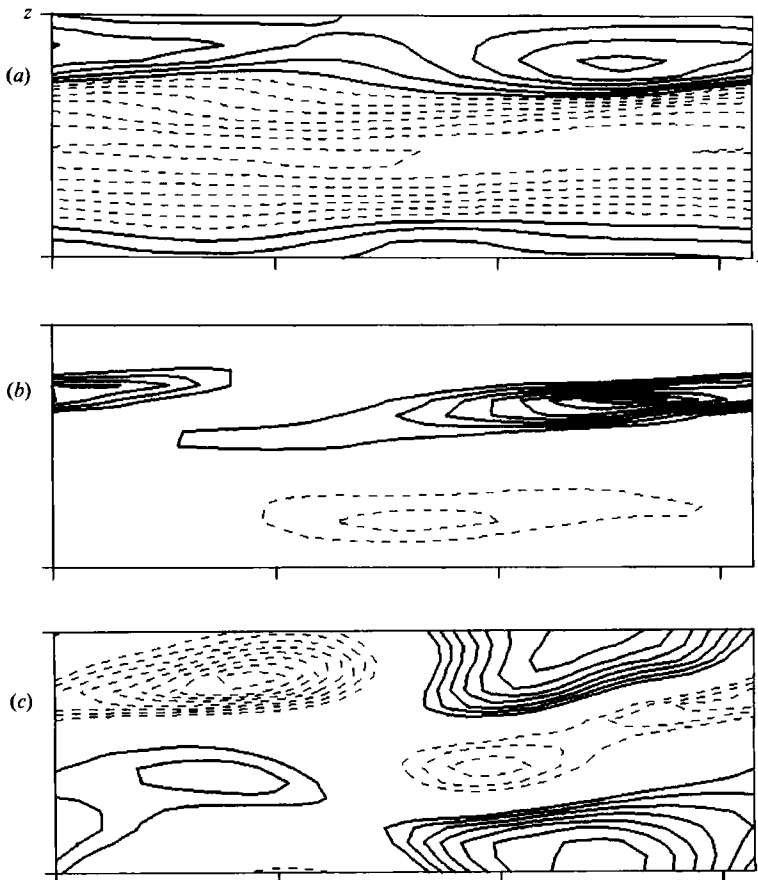


FIGURE 20. Horizontal ( $x, z$ ) section of wall region at  $y^+ = 2.3$ . Flow is from left to right.  $Re = 2000$ , corresponding to  $t = 1187$  in figure 18.  $Re_\tau = 97.7$ ; figure displays whole computational box,  $\lambda_x \times \lambda_z = \pi \times 0.35\pi$ ; (a)  $\omega_z$ ; isoline increment = 0.5. Solid lines:  $\omega_z < -5$ ; dashed:  $-5 \leq \omega_z \leq -2$ . (b)  $\omega_y$ ; isoline increment = 0.1. Solid lines:  $\omega_y \geq 0.3$ ; dashed:  $\omega_y \leq -0.3$ . (c)  $\omega_x$ ; isolines, same as for  $\omega_y$ .

streak that fills the whole central streamwise strip of the computational box. Note that in the immediate vicinity of the wall,  $u \approx -y\omega_z$ , and the contours of  $\omega_z$  indicate the level of streamwise velocity at a fixed  $y$ . In this region,  $\omega_y$  is dominated by  $\partial u / \partial z$ , and the  $\omega_y$  structures indicate the ‘sidewalls’ of the low-velocity streak. Finally, the definition of vorticity and the continuity equation give, near the wall,

$$v \approx \frac{1}{2} \left( \frac{\partial \omega_x}{\partial z} - \frac{\partial \omega_z}{\partial x} \right) y^2, \quad (7)$$

and since the evidence is that in this region  $\partial/\partial x \ll \partial/\partial z$ , the velocity normal to the wall is dominated by the distribution of  $\omega_x$ . The same is true for the other transverse velocity component,  $w$ . This distribution is much less elongated than that of the other two vorticity components, and the section in figure 20 shows two discrete vorticity patches, neither of which extends the full streamwise length of the box. Note that because the computational box is the elementary cell of a two-dimensional periodic arrangement, the positive streamwise vortex that appears in three corners of the figure is actually a single structure, and the basic arrangement of streamwise vorticity is a checkerboard distribution of alternating signs on opposite sides of the

low-speed streak. A better understanding of the geometry can be obtained from figure 21 (plate 1), which is a three-dimensional view of the same field further away from the wall,  $y^+ = 20\text{--}50$ , showing the two streamwise vortices in relation to the low- $\omega_z$  streak. The streamwise vortices are fairly long, filling most of the length of the box, and they are inclined with respect to the wall. The two vortex patches that appear in the sublayer are the ‘roots’ where the longitudinal vortices approach the wall.

A streamwise ( $x, y$ ) section of the  $\omega_z$  field along the centre of figure 20 was shown in figure 11. Its most prominent feature, the strong shear layer protruding from the lower wall, corresponds to similar structures observed previously both experimentally and in numerical simulations (Johansson *et al.* 1987; Jiménez *et al.* 1988). These shear layers are highly three-dimensional, as shown in the ( $y, z$ ) sections of the same field in figure 22(a, b). The two planes for these sections were taken so as to intersect the positive and negative streamwise vortices in figure 20 at their strongest locations. It can be seen that the shear layers protrude from the wall in the streamwise direction and are also inclined across the span. In fact, they are rooted to the sides of the low-vorticity sublayer streak, and their emergence from the wall coincides with the  $\omega_y$  structures in figure 20. Note that the spanwise slopes of the shear layers in the two sections are opposite to one another.

A better understanding of the relation between the two transverse components of vorticity can be gained from figure 22(c, d), which shows vortex traces in the ( $z, y$ )-plane. These are not vortex lines but field lines of the transverse vorticity ( $\omega_z, \omega_y$ ) field, and they represent the intersection with the transverse plane of individual ‘vortex surfaces’, each of which is formed by an array of vortex lines which are not themselves restricted to a given cross-plane. These surfaces are especially meaningful when the streamwise component of vorticity is weaker than the transverse components, in which case their intersections with planes perpendicular to the weaker component provide an indication of the direction and magnitude of the vorticity. This is the case here, where the magnitude of  $\omega_z$  near the wall dominates the other two components (see figure 18b, and the values of the contours in figures 20 and 22). Except for the effect of viscous diffusion, a vortex line belonging to a particular surface stays in it, and the surfaces themselves evolve like material surfaces.

The vortex traces in figure 22(c, d) have been drawn to represent the evolution of the strong layer of transverse vorticity generated by the pressure gradient at the wall, which is the dominant flow feature in the near-wall region. The field lines cover only those points at which the transverse component is large,  $(\omega_y^2 + \omega_z^2)^{1/2} \geq 0.5U/h$ . It is clear from the figure that whenever this layer is lifted away from the wall, it leaves a transverse vorticity ‘gap’ in the wall layer, which is the low-velocity streak. The vortex lines lifting away from the wall at the edges of the gap form the  $\omega_y$  sidewalls of the streak, and the outer boundary of the lifted layer forms the detached shear layers (figure 22a-d). An examination of this figure also provides an explanation for the curious phenomenon of the regions observed near the wall in which  $\omega_z$  has a sign opposite to the mean wall shear. These regions can be observed in both figures 11 and 22(a, b), and cannot be explained in terms of a gradient diffusion process. It is evident from the vortex traces that they represent locations in which the original spanwise vortex layer has been deformed enough to be ‘overturned’, so that the same vortex lines now represent a spanwise vorticity component opposite to its original sign (Jiménez 1988). (We now believe the different explanation of this phenomenon contained in Jiménez *et al.* 1988 to be incorrect.)

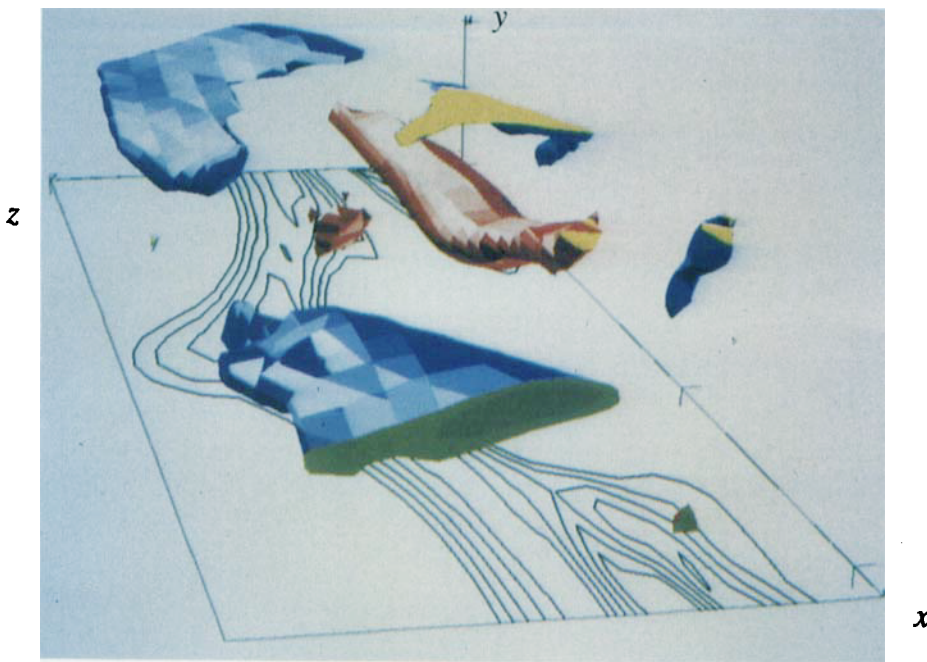


FIGURE 21. Three-dimensional view of the flow field in figure 20. Flow coming out of the page. Horizontal plane is  $y^+ = 10$ , with isolines for  $\omega_z \geq -2.5$  (by 0.25). Surfaces are  $\omega_x = -0.75$  (blue), and  $\omega_x = 1.1$  (red), between  $y^+ = 20$  and 50. Figure displays full horizontal extent of computational box.

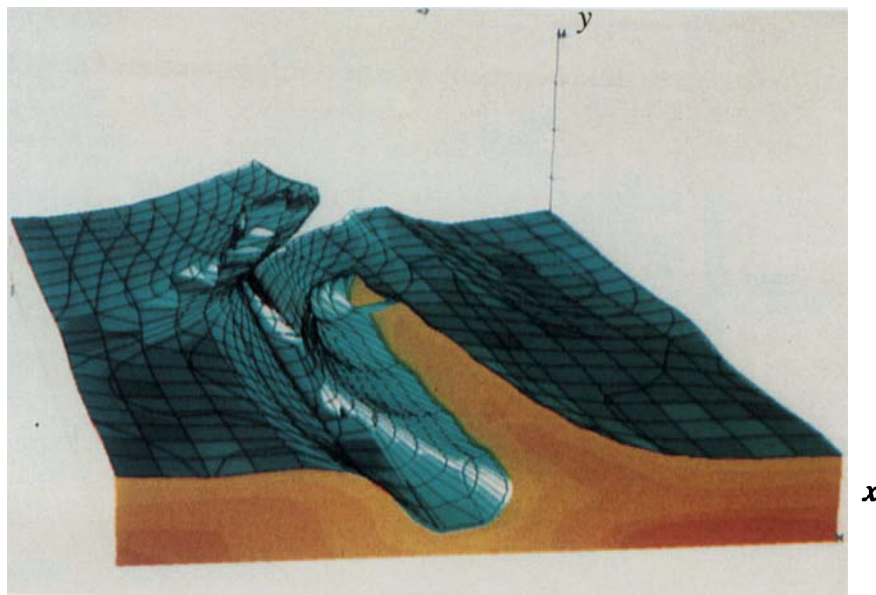


FIGURE 24. Three-dimensional view of  $\omega_z$  region near wall. Flow coming out of the page, corresponding to the field in figures 20–23, between the two sections used for figure 22. Solid surface is  $\omega_z = -2$ .



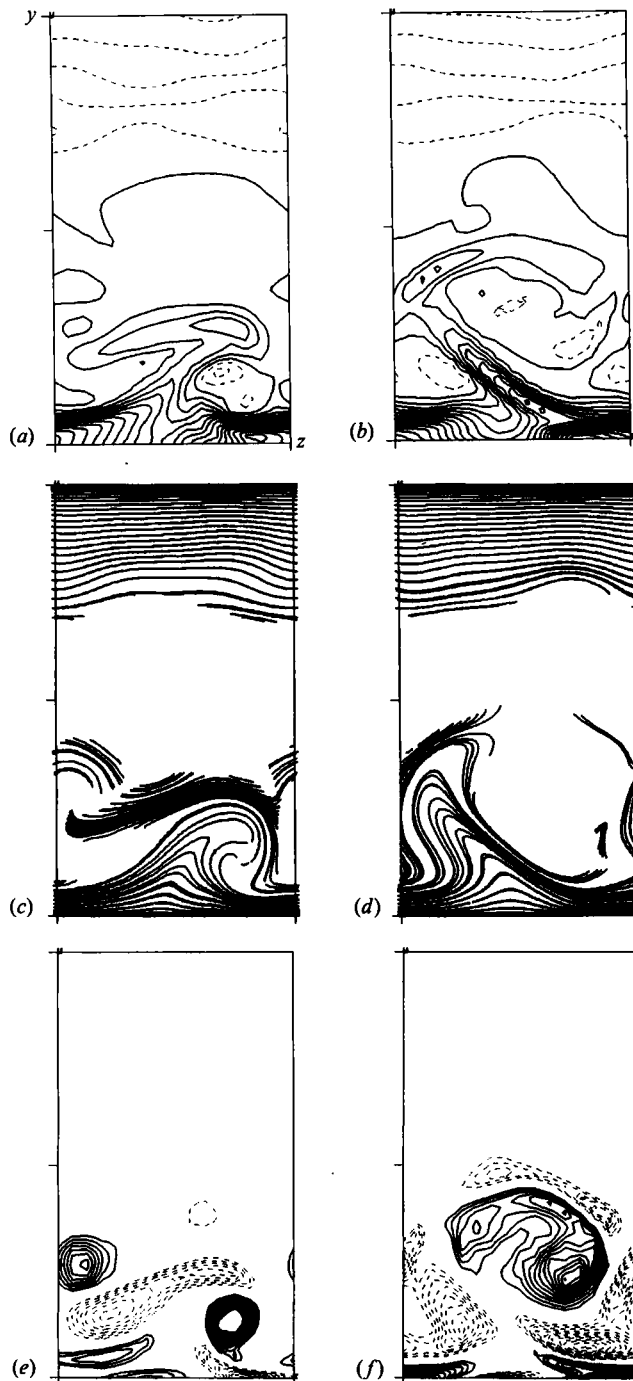


FIGURE 22. Transverse ( $z, y$ ) sections of channel. Field is the same as figure 20. Flow coming out of the page. Figure displays whole computational box,  $\lambda_z \times h = 0.35\pi \times 2$ . (a, c, e)  $x = 0.49$  in figure 20; (b, d, f)  $x = 2.26$ . (a, b)  $w_z$ , Isoline increment = 0.5; solid lines:  $w_z < 0$ . (c, d) Vortex traces, see text. (e, f)  $w_x$ , Isoline increment = 0.1; solid lines:  $w_x \geq 0.3$ ; dashed:  $w_x \leq -0.3$ .

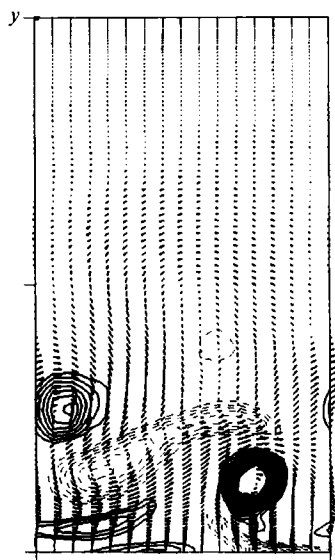


FIGURE 23. Transverse velocities overlaid on the  $\omega_x$  map in figure 22(e).

Figure 22(e, f) contains contours of streamwise vorticity,  $\omega_x$ . There is no clear spanwise symmetrical pairing of opposite signs, but there is a tendency for vortices of opposite sign to stack on top of each other. The probable origin of some of these streamwise vortices can be determined. Net circulation can only be produced by diffusion at the wall, and it is clear from figure 22(a, b) that most of the vorticity in that region is spanwise in accordance with the presence of mean shear. Further from the wall where the large streamwise vortices are located ( $y^+ = 15-40$ ), this is no longer true, and the three vorticity components have comparable magnitudes. Therefore, a likely origin of  $\omega_x$  is the tilting of the original  $\omega_z$  vortex lines. We have already seen that this is the probable origin of  $\omega_y$ . When the streamwise vortices in figure 22 are compared with the transverse vortex traces, it is seen that the sign and position of the large positive vortex in figure 22(f) as well as that of the compact positive vortex in 22(e) and of the two large but more diffuse negative vortices to their left, are consistent with the result of the transverse vortex lines being tilted forward by the prevailing shear. These four regions are just different sections of the two streamwise vortices shown in figure 21. The vorticity peaks at the wall below these large vortices are also easily explained by the diffusion of the wall secondary vorticity required to satisfy the no-slip condition. This leaves part of the streamwise vorticity unexplained, including the two vortices farthest from the wall in both figures. They are probably the result of convection of secondary wall vorticity away from the wall by the primary vortices. This process, in which a vortex near a no-slip wall induces secondary vorticity of opposite sign at the wall, carries it away to generate a new free vortex and then couples with it to form a rising pair, has been nicely demonstrated in two-dimensional computations of vortex dipole rebound by Orlandi (1990). We have also found evidence of the same process, involving single vortices instead of dipoles, during the ‘blooming’ period of the intermittency cycle.

As discussed above, the transverse velocities near the wall are controlled by the distribution of  $\omega_x$ , as is clearly shown in figure 23 in which velocity vectors are overlaid on the vorticity contours of figure 22(e). The transverse velocities in turn contribute to the deformation of the transverse vorticity, and when figures 22(a) and

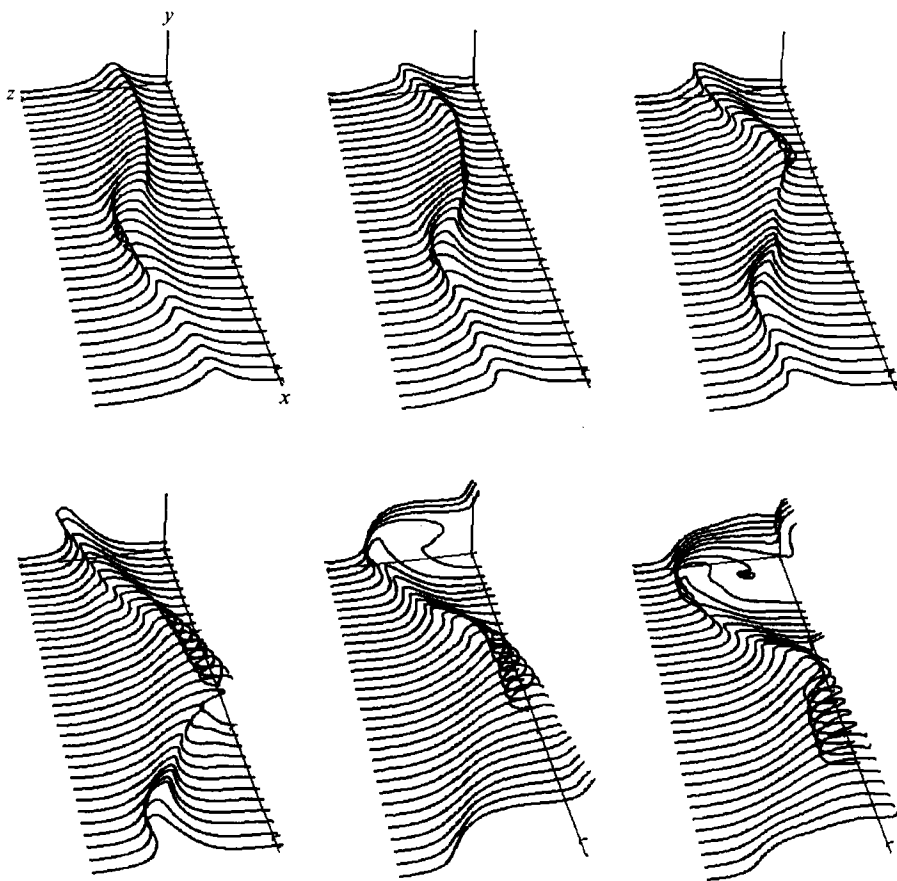


FIGURE 25. Time sequence of the evolution of the wall vorticity layer as it approaches the peak of the intermittency cycle. Conditions are as in figures 22–24. Flow coming out of the page. Vortex surface was based on the left edge of the computational domain at  $y^* = 6$ . Time increases from left to right, top to bottom.  $Ut/h = 1184$  to 1199 by the third frame. Full computational box.

22(d) are considered together, it is apparent that the transverse structure of the flow can be explained as the result of the wall layer being pulled away from the wall by the transverse velocities induced by the streamwise vorticity. The three-dimensional arrangement of the high- $\omega_z$  layer shown in figure 24 (plate 2) clearly shows the detached shear layer being pulled sideways from the wall. The two large streamwise vortices of figure 21 are above the layer, with the positive one located at the right of the picture and the negative one at the rear left. The groove in between is the gap left in the layer by the detached vorticity and constitutes the low-velocity streak.

Since much of the streamwise vorticity can probably be attributed to the forward tilting of the lifted layers, the whole process is very reminiscent of the classical ‘hairpin’ model of transition and turbulence. In this case, however, the hairpin is asymmetric, and only one leg collapses into a compact vortex, while the other one is stretched into a more diffused vortex sheet. Such asymmetric hairpin vortices are typical of natural turbulent boundary layers (Moin 1987). As a consequence, the explosive uplifting due to the formation of symmetric pairs is missing, and the whole structure remains relatively stable for fairly long periods of time. In fact, individual vortices and shear layers can be followed during most of the intermittency cycle,

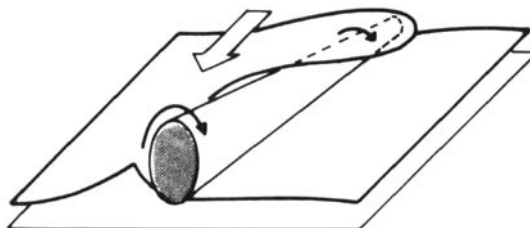


FIGURE 26. Sketch of the lifting of the wall vorticity by an inclined longitudinal vortex. The front edge of the lifted layer appears to move forward as the wrapping continues. Flow coming out of the page.

during which time they are convected downstream for distances of the order of  $x = 100h$ , equivalent to several thousands of wall units. This might be related to the very long streamwise extent of sublayer streaks observed in natural channels.

Figure 25 provides a different view of the lifting of the wall vortex layer by the streamwise vortex. Each frame in the time sequence shows an instantaneous view of the position of the sheet as it approaches the active peak in the second intermittency cycle of figure 18 (§4). The surface is marked by individual transverse vortex traces initiated at  $y^+ \approx 6$  in a relatively undisturbed part of the layer. The lifting of the layer away from the wall over the low-velocity streak is evident, as is the fact that the streak itself is wavy. The frame of reference moves downstream from one frame to the next to keep the roots of the streamwise vortices in the sublayer approximately fixed (convection velocity =  $0.46U$ ). The most striking feature is that the amplitude of the wave in the streak increases and even seems to ‘brake’ in the last two frames of the sequence. This seems to be the nature of the breakdown involved in the ‘blooming’ cycle and was observed to a greater or lesser degree in all of the intermittency cycles that we studied.

The flow field described in conjunction with figures 20–24 corresponds to the second frame in the sequence in figure 25. Recall that there is a compact streamwise vortex rotating clockwise in the page that overlays the lifted streak. In the upstream part of the figure, it lies close to the wall and has rolled the wall layer around itself (figure 22e). This is the part of the wave that bends to the right. In the downstream part of the figure, the sloping vortex lies above the wall layer, is bigger and slower, and has not yet rolled the wall layer. At this point, the layer is pushed left under the vortex, and the streak bends to the left. As time passes, the streamwise vortex continues to wrap the layer, and this happens faster in the upstream region where the core is more compact with stronger rotation (see figure 26). As a consequence, the rightward bend becomes more pronounced and travels forward. This is seen as the travelling kink in the streak in successive frames of figure 25.

Up to this point, the flow field in the neighbourhood of the streak has only a mild streamwise variation, and  $\omega_x$  remains almost steady. It can be easily shown that the stretching and tilting terms in the equation for  $\omega_x$  vanish identically if  $\partial/\partial x = 0$ . As pointed out above, the streamwise vortices probably grow as a result of the forward tilt of the prevailing transverse vorticity. This is a slow process, depending on the deviation from two-dimensionality produced by the undulation of the streak and by the inclination of the vortex away from the wall, both of which are initially small. Eventually, however, the kink in the streak becomes very pronounced. The flow becomes very three-dimensional and the stretching term for  $\omega_x$  suddenly becomes active and creates new streamwise vorticity.

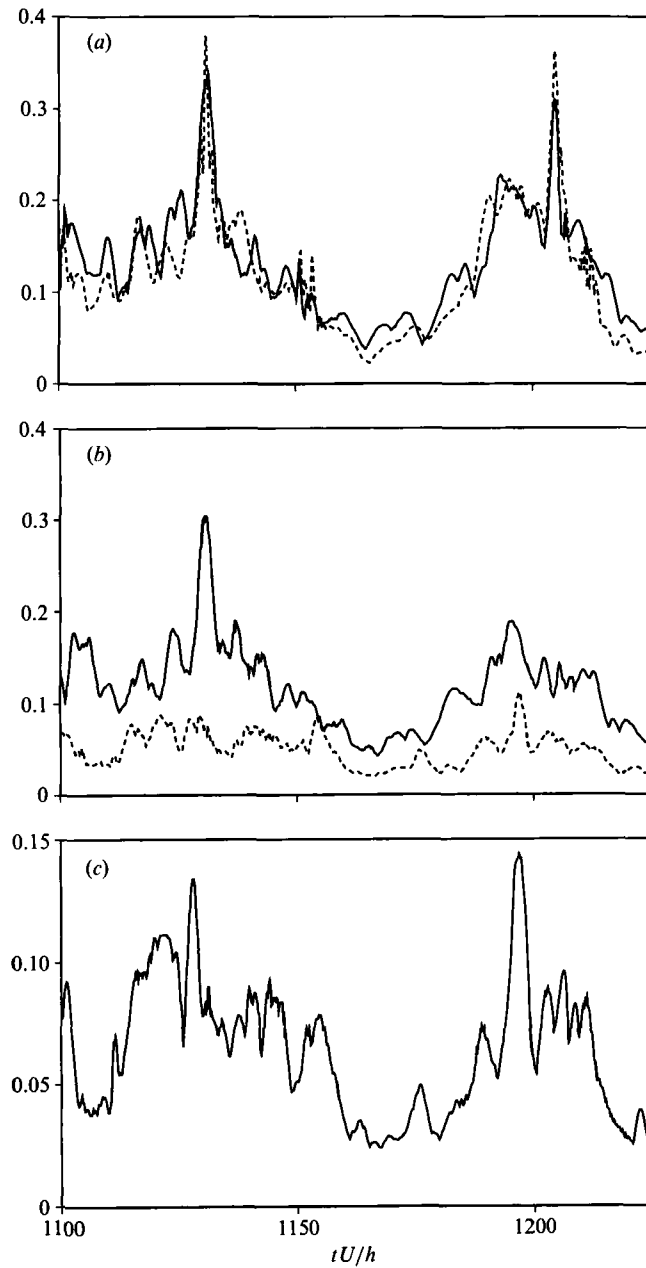


FIGURE 27. Vorticity production terms in the evolution equation for the vorticity (wall units). Time history is same as in figure 18. (a, b) Total time derivative; solid line:  $|D\omega_z/Dt|$ ; dashed:  $|D\omega_x/Dt|$ . (a)  $y^+ \leq 10$ , (b)  $y^+ > 10$ . (c) Tilting and stretching terms for streamwise vorticity:  $\omega \cdot \nabla u$ .

This process can be followed in figure 27, which is a time history of the maximum magnitudes of the total derivatives  $D\omega_x/Dt$  and  $D\omega_z/Dt$  during the intermittency cycle. Figure 27(a) refers to the sublayer,  $y^+ < 10$ , while 27(b) refers to  $y^+ > 10$ . In the sublayer, both derivatives are roughly of the same magnitude and peak sharply during the active part of the cycle. We have determined by direct computation that

the largest contribution in this region is from the viscous terms in the vorticity equation. Outside the sublayer, however, where stretching and diffusion are of the same order,  $\omega_z$  is still very active, while  $\omega_x$  is relatively quiescent as a consequence of the small magnitude of the streamwise derivatives. The stretching term in  $\omega_x$  is active only during the peaks of the cycle when local three-dimensionality is induced by the breaking of the kink on the streak (figure 27c). The details of the three-dimensional interaction are complicated and are still not completely understood. The analysis of a few flow fields suggests that, as the head of the rolled vortex layer overtakes the root of the one just ahead of it, the shear from the front vortex layer acts on the  $\omega_y$  component of the higher one and tilts it forward, creating a new strong  $\omega_x$  vortex that regenerates the cycle. This process is consistent with detailed observations of the *location* of the high- $\partial\omega_x/\partial t$  regions in the flow.

## 6. Conclusions

We have shown that turbulent channel flow can be sustained indefinitely in a computational domain that consists of a strictly periodic two-dimensional arrangement of identical subunits, each of which contains essentially a single set of wall structures. This simplified model, in which the small scales of wall turbulence are well resolved but the long-range decorrelation characteristic of turbulence is not, displayed low-order statistics that are in very good agreement with those of natural turbulent flows, at least below  $y^+ = 40$ . The minimal span and streamwise length of this basic subunit (the minimum critical wavelengths) were determined as the minimum size of the periodic computational box that would sustain turbulence. The minimal spanwise extent was shown to scale in wall variables and to be equal to approximately  $\lambda_z^+ = 100$ . This value has been widely observed as the most probable value for sublayer streak spacing in natural flows, and the present result gives it a dynamical rather than statistical significance. The exploration of the range of streamwise lengths was less extensive than that of spanwise wavelength and the results less conclusive, but the values obtained,  $\lambda_x^+ \approx 250-350$ , are also of the same order as the experimental observations of vortices near a wall. These computational boxes are too small to adequately represent the flow in the outer layer, and the agreement with experiments in that region is poor. Indeed, we found interesting solutions in which turbulence resides only at a single wall for long periods, while the flow at the other wall is relatively quiescent. The fact that the turbulent wall statistics remain fairly good even in those cases indicates a high degree of independence of the flows in the inner and outer regions of the turbulent layers. In the highest-Reynolds-number simulation with very narrow boxes, the near-wall statistics begin to deteriorate, and this coincides with the disappearance of the last traces of a logarithmic region in the mean velocity profile. This confirms the role of the log region as the outer boundary for the near-wall turbulence, and the results summarized above suggests that it may indeed be the only one needed to ensure a correct interaction.

Another interesting result is the identification of a very long,  $Ut/h \approx 100$ , intermittency cycle, during which all of the characteristic turbulent intensities vary strongly. This very long timescale, during which the wall structures are convected several thousand wall units, implies that the structures are very stable, and we suggest that this may be related to the very long streamwise extent of the sublayer streaks observed in experiments. A study of the wall-stress histories in decaying flow fields suggest that this cycle is the regeneration mechanism for the structures in the

wall region and is ultimately responsible for the long-time survival of turbulence in the channel.

We have also identified the structural elements of the vorticity field in each of the basic flow cells. As expected, each computational box contains a single low-speed sublayer streak overlaid by a single detached shear layer of complicated geometry. We have shown that these shear layers are pulled away *sideways* from the wall by the action of a compact streamwise vortex, and that the gap left in the wall vorticity layer as it is lifted is the commonly observed low-speed sublayer streak. Finally, we have identified a mechanism which links all of these elements as they evolve together during the quiescent phase of the intermittency cycle and which is consistent with its long duration. A preliminary model for the active phase of the cycle is also presented.

In summary, we have identified a system that exhibits many of the characteristics of near-wall turbulence in fully developed turbulent channels and that is appreciably simpler than the full channel, and we have used it to study the structure and dynamics of turbulence in the near-wall region. Beyond the specific results of this study, we believe that the simplified system itself will be very useful in future investigations of wall turbulence and its control in a simpler and more economical setting than the full numerical simulation of complete flows.

We are grateful to Drs J. Kim and R. S. Rogallo for helpful comments on a draft of this manuscript.

#### REFERENCES

- BLACKWELDER, R. F. & ECKELMANN, H. 1979 Streamwise vortices associated with the bursting phenomenon. *J. Fluid Mech.* **94**, 577–594.
- BOGARD, D. G. & TIEDERMAN, W. G. 1986 Burst detection with single-point velocity measurements. *J. Fluid Mech.* **162**, 389–413.
- CLARK, J. A. & MARKLAND, E. 1971 Flow visualization in turbulent boundary layers. *J. Hydraul. Div. ASCE* **97**, 1635–1664.
- DEAN, R. B. 1978 Reynolds number dependence of skin friction and other bulk flow variables in two-dimensional rectangular duct flow. *Trans. ASME I: J. Fluid Engng* **100**, 215–223.
- ECKELMANN, H. 1974 The structure of the viscous sublayer and the adjacent wall region in a turbulent channel flow. *J. Fluid Mech.* **65**, 439–459.
- HEAD, M. R. & BANDYOPADHYAY, P. 1981 New aspects of the boundary layer structure. *J. Fluid Mech.* **107**, 297–338.
- HERBERT, T. 1983 Secondary instability of plane channel flow to subharmonic three dimensional disturbances. *Phys. Fluids* **26**, 871–873.
- JANG, P. S., BENNEY, D. J. & GRAN, R. L. 1986 On the origin of streamwise vortices in a turbulent boundary layer. *J. Fluid Mech.* **169**, 109–123.
- JIMÉNEZ, J. 1988 Bifurcations in Poiseuille flow and wall turbulence. In *Proc. AGARD Symp. Fluid Dyn. 3-D Turb. Shear Flows and Transition, Cesme, Turkey, Oct. 3–6*, pp. 15.1–15.11.
- JIMÉNEZ, J. 1990 Transition to turbulence in two dimensional Poiseuille flow. *J. Fluid Mech.* **218**, 265–297.
- JIMÉNEZ, J., MOIN, P., MOSER, R. & KEEFE, L. 1988 Ejection mechanism in the sublayer of a turbulent channel. *Phys. Fluids* **31**, 1311–1313.
- JOHANSSON, A. V., HER, J.-V. & HARITONIDIS, J. H. 1987 On the generation of high-amplitude wall-pressure peaks in turbulent boundary layers and spots. *J. Fluid Mech.* **175**, 119–142.
- KIM, J. & MOIN, P. 1986 Flow structures responsible for the bursting process. *Bull. Am. Phys. Soc.* **31**, 1716.
- KIM, J., MOIN, P. & MOSER, R. 1987 Turbulence statistics in fully developed channel flow at low Reynolds number. *J. Fluid Mech.* **177**, 133–166.

- KLEISER, L. & LAURIEN, E. 1985 Three dimensional numerical simulation of laminar-turbulent transition and its control by periodic disturbances. In *Laminar-Turbulent Transition* (ed. V. V. Korlov), pp. 29–37. Springer.
- KLINÉ, S. J. & AFGAN, N. H. 1988 *Near Wall Turbulence*, Proc. 1988 Zorac Zaric Mem. Conf. Hemisphere.
- KLINÉ, S. J., REYNOLDS, W. C., SCHRAUB, F. A. & RUNDSTADLER, P. W. 1967 The structure of the turbulent boundary layer. *J. Fluid Mech.* **30**, 741–773.
- MAY, C. L. & KLEISER, L. 1985 Numerical simulation of subharmonic transition in plane Poiseuille flow. *Bull. Am. Phys. Soc.* **30**, 1748.
- MOIN, P. 1987 Analysis of turbulent data generated by numerical simulations. *AIAA Paper 87-0194*.
- MOIN, P. & KIM, J. 1985 The structure of the vorticity field in turbulent region flows. Part 1: Analysis of instantaneous fields and statistical correlations. *J. Fluid Mech.* **155**, 441–464.
- NISHIOKA, M. & ASAI, M. 1985 Some observations of the subcritical transition in plane Poiseuille flow. *J. Fluid Mech.* **150**, 441–450.
- ORLANDI, P. 1990 Vortex dipole rebound from a wall. *Phys. Fluids A* **2**, 1429–1436.
- PATEL, V. C. & HEAD, M. R. 1969 Some observations on skin friction and velocity profiles in fully developed pipe and channel flows. *J. Fluid Mech.* **38**, 181–201.
- SANKARAN, R., SOKOLOV, M. & ANTONIA, R. A. 1988 Substructures in a turbulent spot. *J. Fluid Mech.* **197**, 389–414.
- SMITH, C. R. & METZLER, S. P. 1983 The characteristics of low-speed streaks in the near wall region of a turbulent boundary layer. *J. Fluid Mech.* **129**, 27–54.
- WEI, T. & WILLMARTH, W. W. 1989 Reynolds-number effects on the structure of a turbulent channel flow. *J. Fluid Mech.* **204**, 57–95.
- ZHANG, Z. & LILLEY, G. M. 1981 A theoretical model of the coherent structure of the turbulent boundary layer in zero pressure gradient. In *Proc. 3rd Symp. Turb. Shear Flows*, Davis, CA, Sept. 9–11, pp. 11.24–11.29.